Undulator radiation for at-wavelength interferometry of optics for extreme-ultraviolet lithography

David Attwood, Gary Sommargren, Raul Beguiristain, Khanh Nguyen, Jeffrey Bokor, Natale Ceglio, Keith Jackson, Masato Koike, and James Underwood

Techniques are described for at-wavelength interferometry of multilayer coated optics designed for use in extreme-ultraviolet lithography. Broadly tunable undulator radiation, which covers the spectral region from 45 to 400 Å, is described. The coherent power available at these wavelengths is described, and several types of interferometer that might be suitable at these short wavelengths are also described.

Introduction

The use of soft-x-ray (SXR) and extreme-ultraviolet (EUV) radiation is opening new opportunities in microscopy, lithography, and astronomy.[1] Radiation at these short wavelengths has recently been used in a diverse array of experiments, from basic materials[2] and biological sciences to integrated circuit lithography.[3] Many of the recent experiments take advantage of multilayer coated optics with high normal-incidence reflectivity. Reflectivities of greater than 60% have been obtained at the 130-Å wavelength at several laboratories.[4–6] Capabilities for optical coatings at even shorter wavelengths continue to advance but present a significant challenge to material scientists as the individual coating layer thicknesses, approximately $\lambda/4$ at normal incidence, are measured in atomic dimensions. Recent developments include the achievement of 20% reflectivity at the 70-Å wavelength on flat and moderately curved substrates.[7,8]

A further challenge is to extend near-diffraction-limited performance to large numerical-aperture, large-field-of-view reflective optics at those same wavelengths. The need for such a capability is particularly evident in the case of EUV lithography for future nanoelectronic devices, for which 0.1-μm features will be required over field sizes measured in square centimeters for gigabit memory devices.[9] The successful development of these capabilities will enhance pursuits of short-wavelength reflective optics in other areas of science and technology. The combined need for near-diffraction-limited EUV imaging and a large field of view will clearly require an extension of present techniques for optical surface preparation. More demanding tolerances will be set for both surface contour and roughness, and new test procedures will be required for assessing progress toward successful optical fabrication and polishing. To maintain $\lambda/4$ peak-to-valley wave-front distortions in an optical system with four reflecting surfaces would typically require contour variations limited to $\lambda/16$,[10,11] or ~8-Å surface variations for a 130-Å wavelength. Surface roughness should be held below 1–2 Å rms because of its effect on reflectivity in these short-period coatings.

Here we discuss the need for accurate interferometric testing of EUV optics (and, incidentally, microscope and telescope optics designed to have diffraction-limited or near-diffraction-limited SXR performance) at the wavelength at which they are expected to operate. We call this *at-wavelength* interferometry. In particular we discuss the appropriate source of radiation for this kind of interferometry. At-wavelength EUV interferometry will be an important tool to detect and quantify local contour variations to 8 Å or less and to assess further phase distortions within the coatings that are due to local variations in material densities, spacings, and interface orientation.

Ultimately visible-light metrology of EUV optical component substrates will probably also be required

G. Sommargren and N. Ceglio are with the Advanced X-Ray Optics Group, Lawrence Livermore National Laboratory, Livermore, California 94550. The other authors are with the Center for X-Ray Optics, Lawrence Berkeley Laboratory, University of California, Berkeley, California 94720.

Received 3 November 1992.
0003-6935/93/347022-10$06.00/0.

for use by optical technologists to monitor the surface figure during the fabrication process. The main motivation for this is that any at-wavelength testing will depend on the use of some sort of reflective coating. In the fabrication process, many iterations of polishing and testing are used, and thus the need to deposit and remove coatings repetitively would make at-wavelength testing impractical. However, the absolute accuracy of present state-of-the-art visible phase-measuring interferometry will need to be improved by a factor of 10–20 in order to achieve the accuracy necessary to characterize EUV imaging systems. Significant research and development will be required for achieving this advance. In support of this goal, it is clear that at-wavelength metrology has a crucial role to play. As mentioned above, an absolute surface accuracy of ~ 8 Å is required on substrates for diffraction-limited EUV imaging systems. With an EUV interferometer, this would represent a required measured accuracy of $\sim \lambda_{EUV}/16$, which appears to be feasible. Designs for such an interferometer are discussed below. This instrument would be extremely useful in support of the research and development efforts to improve the accuracy of visible testing instruments. For example, using an EUV metrology facility, spherical reference surfaces, and special test artifacts could be qualified at the required level of accuracy. These could then be used as reference optics in a visible-light interferometer or as calibration objects for measurement and analysis of systematic effects in the visible interferometer.

Functional testing at the operational wavelength will also be required when the optical component substrates are to be coated, aligned, and installed in their operational configuration in the EUV optical system. This is because the EUV coatings themselves, being interference devices, behave completely differently at their design wavelength than they do in visible light, for which they act as broadband mirrors. In particular, phase effects that might arise from nonuniformity of the layer materials or thicknesses, departures from desired period variations, stresses in the layers, or modification of the top surface by oxidation or contamination[12] will not be correctly evaluated by visible interferometry, yet they have the potential to degrade the system performance seriously. The question of distortion of the optics beyond an acceptable figure error by stresses in the coatings must also be considered. In the visible spectral region, it has been found that the stresses in multilayer coatings are sufficient to bend even thick optical elements an appreciable fraction of a wavelength,[13,14] and it is known that EUV reflecting multilayer coatings develop very large stresses.[15] A sensitive method of measuring these distortions will be essential.

We can estimate the coherent power needed for this application based on a given interferometer design. Calculations for a proposed design are presented below. The common considerations in these estimates are the need for parallel detection in a many-pixel-array detector for fringe visualization and rapid data-acquisition time to minimize image degradation by vibration and drift as well as an allowance for real-time system alignment and the relatively low efficiency of EUV optical components. For the interferometer designs considered, measurements within an exposure time of a second or less will require a coherent power in the range of a fair fraction of 1 W.

Toward this end, undulator radiation at a modern storage ring is particularly interesting. Such radiation, generated by the passage of relativistic electrons through a periodic magnet structure, is readily produced at both EUV and SXR wavelengths, is broadly tunable, and is partially coherent to a useful degree at these wavelengths. In the following sections we describe undulator radiation further, preliminary designs for EUV interferometry, and give an estimate of anticipated exposure time. Comparison with the coherence properties of other sources is included along with order of magnitude exposure times.

Undulator Radiation

Undulator radiation is emitted by highly relativistic electrons as they traverse a periodic magnetic structure of moderate magnetic-field strength. Such radiation is a major attribute of modern synchrotron facilities, which combine many such magnetic structures with a tightly controlled electron beam. By choosing the magnetic structure period and electron energy, one can center the radiation at wavelengths from the ultraviolet to the x-ray region. The relative spectral bandwidth of undulator radiation, $\Delta\lambda/\lambda$ is nominally equal to the inverse of the number of magnet periods traversed N, that is, to the number of electron oscillations, typically 60 for the structures being considered. This bandwidth can be substantially narrowed to values of the order of 10^{-4} through the use of a grating monochromator, but at a concomitant reduction of available photon flux. The tuning range of an undulator is very broad, from 45 to 400 Å for the structures of interest here. This continuous tuning is accomplished by varying the magnet gap, thus varying the magnetic-field strength, which controls the electron transit time and thus the temporal duration of the N oscillations. In addition to these spectral features, undulator radiation can have very interesting coherence properties, depending on the degree to which the electron beam is constrained in its lateral size and random angular motion, e.g., depending on the phase-space properties of the electron bunch. A striking feature of the newest facilities is the very small phase space of the electron bunch, which is comparable with that of diffraction-limited radiation at very short wavelengths, of the order of 100 Å. As a consequence, the emitted undulator radiation is partially coherent in nature. With modest spatial and temporal filtering, this radiation is ideally suited for sophisticated experimentation based on the use of well-controlled phase distributions at very short wavelengths.

Figure 1 illustrates the generation of undulator radiation by relativistic electrons traversing a peri-

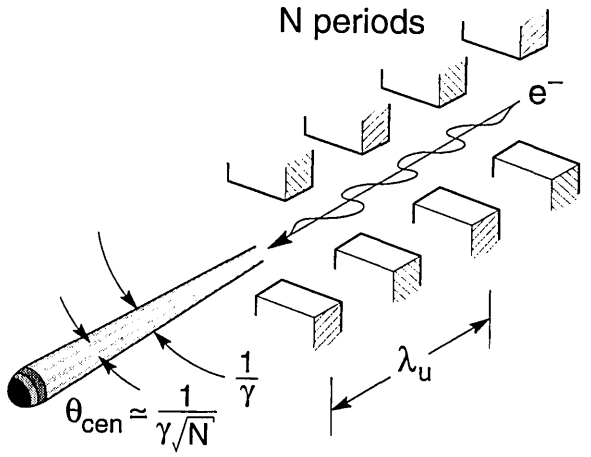

Fig. 1. Continuously tunable short-wavelength undulator radiation is generated by the passage of relativistic electrons through a periodic magnet structure.

odic magnet structure.[16–18] The observed wavelength is described by the equation

$$\lambda_x = \frac{\lambda_u}{2\gamma^2}\left(1 + \frac{K^2}{2} + \gamma^2\theta^2\right), \tag{1}$$

where λ_u is the undulator period, $\gamma = 1/[1 - (v^2/c^2)]^{1/2}$ is the Lorentz contraction factor familiar from studies of relativistic motion, v is the axial electron velocity, c is the velocity of light in vacuum, θ is the observation angle measured from the axis of symmetry, and K is a dimensionless measure of the magnetic field in a periodic structure,[17] given by

$$K = \frac{eB_o\lambda_u}{2\pi mc}. \tag{2}$$

B_o is the maximum magnetic-field strength on axis, and e and m are the electron charge and the rest mass, respectively.

Typical parameters of interest here[19] include an 8-cm magnetic period, $\gamma \approx 3000$, and K varying from 0.5 to 3.9. This gives a broad tuning range extending from 45 to 400 Å. A typical value for the relative spectral bandwidth is

$$\frac{\Delta\lambda}{\lambda} \cong \frac{1}{N}, \tag{3}$$

where N is the number of magnetic periods (electron oscillations), ~ 0.016 for a 4.96-m-long undulator with 62 periods of 8.0 cm each. This can be accomplished with a simple aperture of angular acceptance,

$$\theta_{cen} = \frac{1}{\gamma^*\sqrt{N}}, \tag{4}$$

where the asterisk denotes a modified Lorentz factor,

$$\gamma^* = \gamma\Big/\left(1 + \frac{K^2}{2}\right)^{1/2},$$

which accounts for the decreased axial velocity in a periodic magnetic field (where a portion of the conserved energy is directed to transverse motion). The central radiation cone, of half-angle θ_{cen}, contains to first order the radiation of bandwidth $1/N$. To obtain radiation with a narrower spectral bandwidth, a monochromator must be used, albeit with reduced photon flux because of both the narrower bandwidth and the finite efficiency of the various components.

The average power radiated in the central radiation cone is readily determined[16] in analytic form from considerations of classical dipole radiation and appropriate use of Lorentz transformations for the case of $K \lesssim 1$. For K substantially larger than 1, numerical simulations are required because strongly nonsinusoidal motion sets in and because the dipole approximation begins to fail. For modest field strength ($K \lesssim 1$) the power in the central cone ($\theta_{cen} = 1/\gamma^*\sqrt{N}$, $\lambda/\Delta\lambda \cong N$) can be written as

$$P_{cen} \cong \frac{\pi e K^2\gamma^2 I}{\epsilon_0\lambda_u\left(1 + \frac{K^2}{2}\right)^2}, \tag{5}$$

where ϵ_0 is the permittivity of free space, and I is the average current. As used here, expression (5) represents only that power radiated in the fundamental ($n = 1$). At the Advanced Light Source (ALS), currently under construction at the Lawrence Berkeley Laboratory, where a current of 0.4 A is expected at $\gamma = 2940$, expression (5) indicates that a central cone power of ~ 1.1 W can be expected within a 1.6% relative spectral bandwidth ($1/N$) at $\lambda = 130$ Å from an 8.0-cm undulator operated at a magnet strength corresponding to $K = 1.9$. Numerical simulations[20] show the radiated power at $K = 1.9$ to be 0.93 W at 130 Å in a spectral pattern that is approximated by $\Delta\lambda/\lambda = 1/N$. Figure 2 graphs power in the central radiation cone ($n = 1$, $\Delta\lambda/\lambda \simeq 1/N$), according to expression (5), through typical tuning ranges of 5.5- and 8.0-cm periodic undulators at the ALS. Because both magnetic structures are constrained to 5-m total lengths, values of N and thus of nominal values of $\Delta\lambda/\lambda$ differ for the two cases, as indicated by expression (3). Thus, although the powers are quite similar, the powers per unit bandwidth are not. Note that the conversion from wavelength to photon energy ($E = \hbar\omega$) is

$$E\lambda = 12{,}399 \text{ eV Å}. \tag{6}$$

For K values greater than unity, electron motion in a periodic magnetic structure becomes nonsinusoidal, that is, the motion becomes more complex than a single frequency, exhibiting ever larger components of multiples of the fundamental frequency. That is, the motion has significant harmonic content for $K > 1$ and radiates accordingly into harmonics of wavelength λ/n with interesting polarization and phase effects. Numerical simulations that account for the nonsinusoidal motion at a high K value and for the

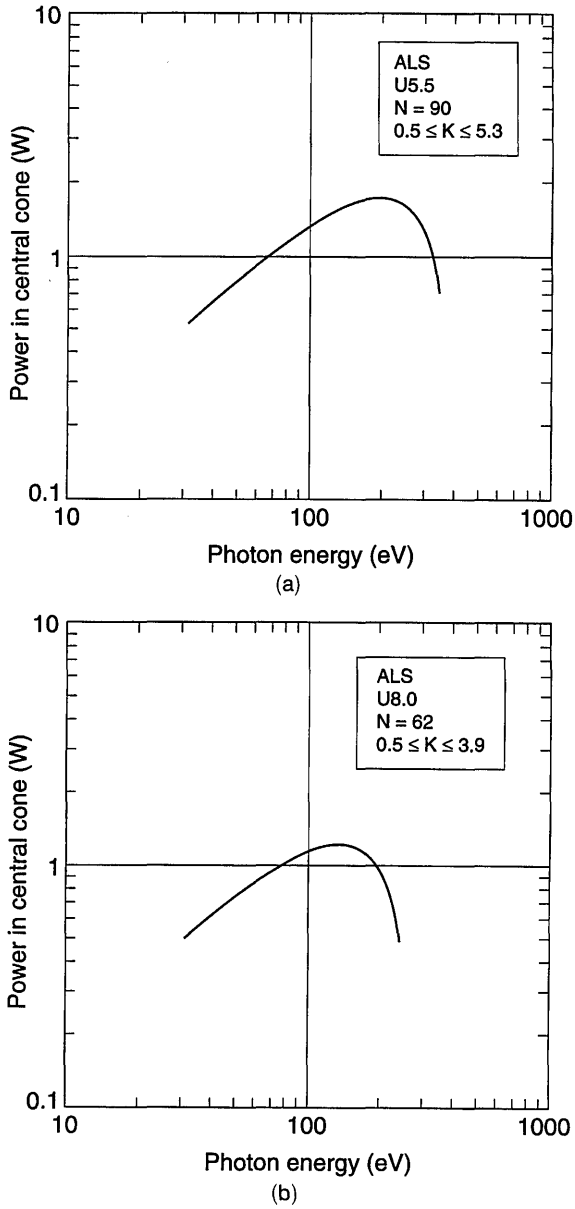

Fig. 2. Power anticipated in the central radiation cone ($n = 1$, $\Delta\lambda/\lambda \simeq 1/N$) as a function of photon energy for (a) 5.5-cm and (b) 8.0-cm period undulators at the ALS, a 1.5-GeV electron storage ring. Note that $\Delta\lambda/\lambda$ is different in the two cases because of differences in N.

finite electron-beam size and divergence provide a more accurate description of the anticipated harmonic content and spectral shape than the simple theory leading to expression (5). Figure 3 shows the harmonic spectrum anticipated[20] at the ALS from both 5.5- and 8.0-cm periodic undulators, each for two selected values of K corresponding to fundamental ($n = 1$) wavelengths of 130 and 70 Å. These two cases are quite interesting; although both generate just under 1 W at 130 Å, the spectral bandwidth is narrower ($1/N$) for the 5.5-cm device, but its K value is higher (2.5 versus 1.9), leading to additional power in harmonics. Although valuable in some situations, the additional power essentially serves as an unwanted heat load on beam-line optics for the interferometry of interest here, e.g., 649-W total power radiated to all angles and wavelengths for the $U5.5$ versus 180 W for the $U8.0$. In practice, harmonics of $n > 5$ will be significantly reduced by the effects of magnetic errors and finite energy spread in the electron beam.[21,22] Further analysis, including the effect of thermal loading on precision optical surfaces, is required before an optimum choice is made. It is clear, however, that both undulators would provide substantial power across the tuning range in a spectral bandwidth appropriate for studies of coated optics.

Coherent Radiation

Interferometry, a powerful diagnostic tool, is particularly useful when used with spatially and temporally coherent radiation, which permits high-contrast fringe formation with a very flexible arrangement of optical surfaces, surface curvature, etc. Undulator radiation has interesting properties of partial coherence that, with appropriate spatial and temporal filtering, render it very useful for at-wavelength interferometry of EUV coated optics and optical systems. To obtain a measure of the coherence properties, we compare undulator radiation with that of a point-source radiator oscillating at a well-defined frequency for a very long time. Clearly our goal is to obtain relations that give us some measure of how small our point source must be and how many oscillation periods are required for generating spherically propagating waves in which phase relationships are preserved across sufficiently large lateral and longitudinal dimensions to be useful in very generally conceived interferometric geometries. The logic of this limiting case argument is that if the source appears to be a point source it cannot reveal detailed phase and intensity variations and thus appears only as propagating spherical waves within the limits of finite observation angle and wavelength.

To estimate how small our equivalent point source must be, Heisenberg's uncertainty principle is utilized for transverse position and momentum, $\Delta\mathbf{x} \cdot \Delta\mathbf{p} \geq \hbar/2$, where these are assumed to be radial rms measures of Gaussian distributions.[23] To put this into a convenient form, we associate the uncertainly in position $\Delta\mathbf{x}$ from which a photon emerges with a source of diameter d, where $d = |2\Delta\mathbf{x}|$. For radiation that is nearly monochromatic we associate the uncertainty of photon transverse momentum $\Delta\mathbf{p}$ with the half-angle of the radiation cone θ, that is, we take $\Delta p \approx |\mathbf{p}| \cdot \theta = \hbar k\theta = 2\pi\hbar\theta/\lambda$. Combining these in the uncertainty relation, we obtain

$$d\theta \geq \frac{\lambda}{2\pi} \tag{7}$$

as the limiting condition for the generation of spatially coherent radiation in which phases are strongly correlated laterally across the radiation field. Recall that d and θ are rms, or $1/\sqrt{e}$ quantities. Note that

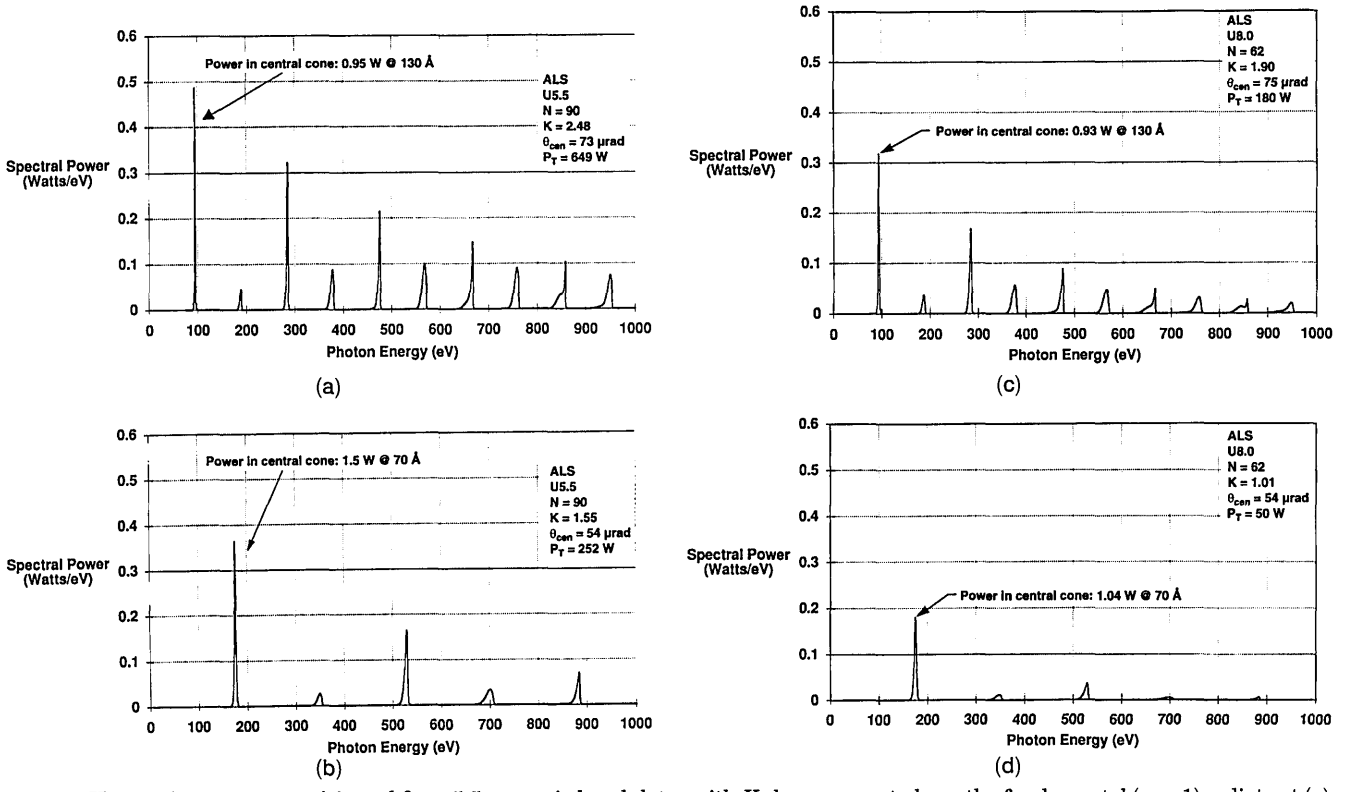

Fig. 3. Harmonic spectrum anticipated for a 5.5-cm period undulator with K chosen so as to have the fundamental ($n = 1$) radiate at (a) 130 Å and (b) at 70 Å. (c), (d) The spectrum for an 8.0-cm period undulator radiating in the fundamental wavelengths of 130 and 70 Å, respectively.

relation (7) describes the relation between the waist diameter and the far-field divergence half-angle for a TEM_{00} laser mode,[24] that is, a spherically propagating wave with a Gaussian intensity distribution. We now have a convenient measure [relation (7)] against which to compare sources of radiation for their potential use in experiments benefiting from the use of spatially coherent radiation.

Temporal coherence is generally described in terms of a coherence length, that is, a propagation distance over which longitudinal phase relations are maintained to a certain degree of accuracy. For instance, one can define a coherence length,

$$l_{\mathrm{coh}} = \frac{\lambda^2}{2\Delta\lambda}, \tag{8}$$

which gives a measure of acceptable path mismatch over which fringe visibility is maintained, as a product of the wavelength λ and the number of oscillation periods $\lambda/\Delta\lambda$, to some numerical factor of the order of 2, which depends on spectral shape and definitions.[25]

For undulator radiation at modern storage rings[26] such as the ALS, the phase-space product of electron-beam diameter d and radiation cone half-angle θ approach the values given by relation (7). The electron beam at the ALS is expected to be elliptical in shape, with a horizontal major axis of $2\sigma_h = 660$ μm and a vertical minor axis of $2\sigma_v = 126$ μm. The central radiation cone half-angle for a single electron, given by Eq. (4), is ~75 μrad for the 8.0-cm period undulator and ~53 μrad for the 5.5-cm period undulator. Random angular divergences within the electron beam increase, to some degree, the effective radiation cone angle. At the ALS, the random electron-beam divergence is expected to be $\sigma_v' = 16$ μrad and $\sigma_h' = 30$ μrad half-angles in the vertical and the horizontal planes, respectively. Combining these quantities gives a slightly elliptical radiation cone of 77-μrad half-angle in the vertical plane and 81 μrad in the horizontal plane. Comparing these values of $d\theta$ with the spatial coherence limit given by relation (7), we find that undulator radiation at 130 Å will be ~4.7 times diffraction limited in the vertical plane and ~26 times diffraction limited in the horizontal plane.[27] Thus spatial filtering will reduce available power by an overall factor (4.7 × 26) of ~120. With a central radiation cone power of 1.1 W for the 8.0-cm periodic undulator, this indicates a spatially coherent power of 9.2 mW at 130 Å. The average coherent power, within a nominal $1/N$ bandwidth, can thus be written as the power in the central cone [expression (5)] reduced by the fraction of radiation having its phase-space product $d\theta$ within the spatially coherent limit $\lambda/2\pi$ set by relation (7) in both the horizontal and the vertical planes, viz.,

$$P_{\mathrm{coh}} = P_{\mathrm{con}} \frac{(\lambda/2\pi)^2}{(d\theta)^2_{h,v}} \tag{9}$$

where $(d\theta)^2_{h,v}$ is shorthand for the product of $(d\theta)_h$ and $(d\theta)_v$ evaluated separately for the horizontal and the vertical planes.

For the $U8.0$ periodic undulator with $N = 62$, the spatially coherent radiation would have a longitudinal coherence length [Eq. (8)] of $l_{coh} = \lambda^2/2\Delta\lambda = N\lambda/2 \simeq 0.40$ μm at $\lambda = 130$ Å. If a longer coherence length were desired, a monochromator[28] could be introduced, but with a concomitant loss in power. For instance, if a monochromator of relative spectral bandwidth $(\Delta\lambda/\lambda)_M \simeq 10^{-3}$ were utilized to probe the coated optics with a spectral bandwidth much narrower than the coating bandwidth, this would make use of a narrower fraction of available bandwidth from the undulator central cone by a factor $N(\Delta\lambda/\lambda)_M \simeq 0.062$ for the 8.0-cm periodic undulator but would provide a longer coherence length of 6.5 μm at $\lambda = 130$ Å. Because of the proportionately reduced photon flux and an additional insertion loss ($\eta_M \simeq 1/3$) that is due to monochromator grating efficiency and mirror reflectivities, the coherent power would be reduced to ~0.2 mW at 130 Å. Figure 4 shows the coherent power tuning curves for both the $U8.0$ and $U5.5$ undulators assuming use of a 10^{-3} relative spectral bandwidth monochromator with a factor of 3 insertion loss that is due to finite efficiencies.

Undulator radiation at older synchrotron facilities could also be used for these purposes, but with reduced coherent power and increased exposure times, because of their larger electron-beam size and divergence. Spatially filtered radiation could also be used from a laser-produced plasma at 130 Å, but the phase space would be very large. For example, if a high-power laser operating at a sufficient repetition rate could put an average of 500 W of visible light at high intensity ($\geq 10^{11}$ W/cm^2 per pulse) onto an appropriate target material with an energy conversion[29] efficiency of 1% into a 3% bandwidth at 130 Å, this would yield ~5 W of power at 130 Å in a relative spectral bandwidth $\Delta\lambda/\lambda \simeq 3\%$. For a plasma source size $d \simeq 200$ μm and an rms radiation half-angle $\pi/4$, the phase-space product $d\theta$ would be approximately 8×10^4 in both the horizontal and the vertical planes. The spatially coherent power would thus be 5 W/$(8 \times 10^4)^2 \simeq 1$ nW in a 3% relative bandwidth. Utilizing the same monochromator to achieve a longer 6.5-μm coherence length and narrower spectral probe, $(\Delta\lambda/\lambda)_M \simeq 10^{-3}$, would result in a coherent power of 30 pW at 130 Å, a factor of ~10^7 less than that for an undulator at the ALS.

Interferometry

Even with the relatively high temporal and spatial coherence afforded by the undulator, interferometry is by no means a simple proposition. Because the wavelength is approximately 50 times smaller than that used in visible interferometry, vibration and long-term stability are of the utmost concern. For instance, if the angular alignment of two nominally parallel interfering wave fronts is changed by as little as 1 mrad, the fringes formed will be spaced by 13.0 μm, unresolved by most EUV–CCD array detectors. And if optical path differences exceed the coherence length, the fringe visibility will drop to zero, making measurements impossible. It would therefore be advantageous to work with interferometer configurations that are inherently immune to these effects.

There is a class of interferometers[30,31] called common path interferometers that meet these needs. In these interferometers, the reference and the measurement wave fronts travel essentially the same path through the interferometer, including the optical component or system under test. This approach, at least to first order, eliminates vibration and drift and ensures near-zero optical path differences.

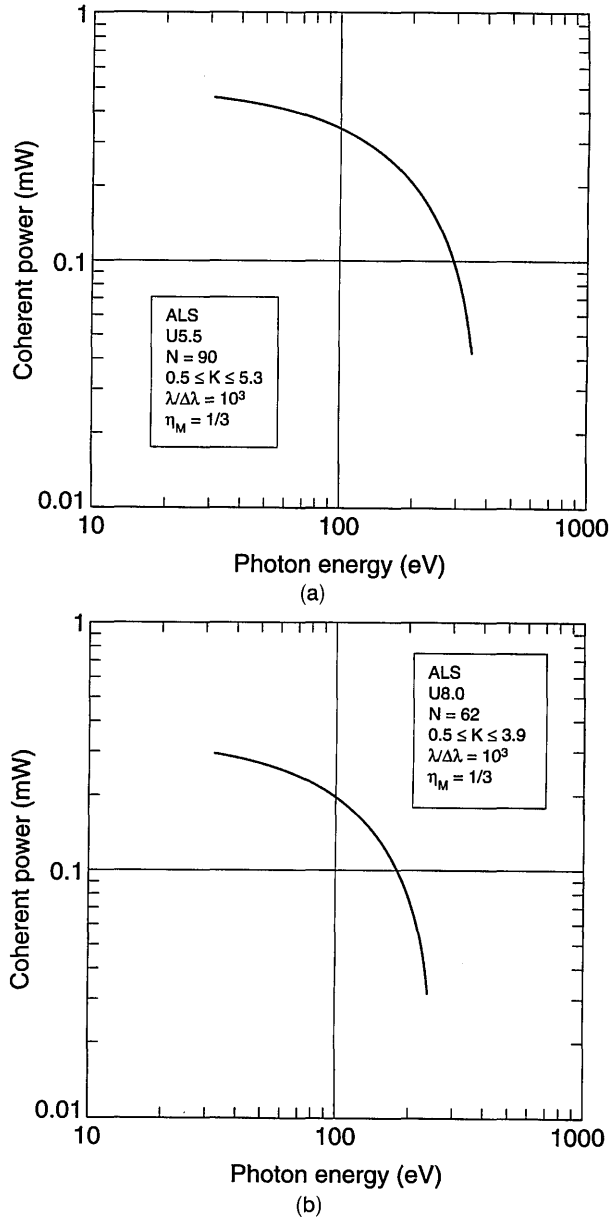

Fig. 4. Predicted coherent power tuning curves for (a) 5.5-cm and (b) 8.0-cm period magnet structures at the ALS. These curves assume use of pinhole spatial filtering, use of a monochromator of relative spectral bandpass $\Delta\lambda/\lambda = 10^{-3}$, and a monochromator efficiency of 33%,

Shearing interferometers are one group of interferometers within this class. They have the characteristic that the reference and the measurement wave fronts are equally affected by the aberrations of the optical component or system under test. They produce an interference pattern by interfering the aberrated wave front with a sheared duplicate of itself. They can take many forms, with lateral and radial shears the most easily implemented. Figure 5 shows a grating lateral shearing interferometer[32] that can operate with a minimal coherence length. The aberrated wave front from the mirror under test comes to focus on a two-frequency grating. Two first-order diffracted wave fronts produced by the grating are laterally sheared with respect to each other. The interference pattern formed is related to the gradient of the aberration in the direction of the shear. These interferometers, therefore, do not give a direct measurement of the aberrations. They require computational analysis for reconstructing the aberrations, usually with some degradation of the results. Because the wave fronts are sheared, there must be sufficient spatial coherence to ensure high visibility fringes. The effective source size should be smaller than d/s times the resolution of the optical component or system under test, where d is the diameter of the wave front and s is the maximum shear.

Another group of interferometers is configured such that the reference wave front is affected by only a very small portion of the optical component under test. These interferometers include scatter plate, zone plate,[33] and some birefringent interferometers. At EUV wavelengths, only the zone plate interferometer is practical. One configuration is shown in Fig. 6. A zone plate is placed at the center of curvature of the mirror under test, and the undulator beam is focused onto the center of the mirror. The undiffracted (zero-order) beam illuminates only a very small portion of the mirror and serves as the reference wave front. The first-order diffracted beam illuminates the entire mirror and serves as the measurement wave front. When these wave fronts are reflected back to the zone plate they are each diffracted a second time. To ensure good fringe visibility in the interference pattern, the interfering wave fronts must be of nearly equal intensity. This is

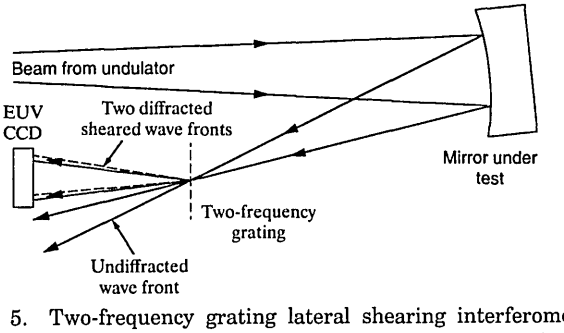

Fig. 5. Two-frequency grating lateral shearing interferometer testing a concave mirror. The interference pattern formed by the two first-order diffracted wave fronts is related to the gradient (in the direction of the shear) of the mirror aberration.

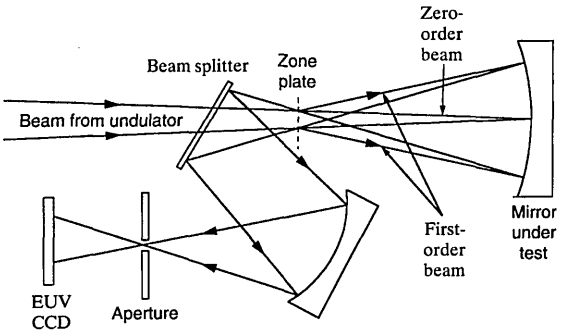

Fig. 6. Zone plate interferometer testing a concave mirror. The interference pattern is formed by the (0, 1) diffracted wave front (reference) and the (1, 0) diffracted wave front (measurement).

accomplished by the use of an aperture that transmits only the reference wave front that is diffracted into the first order and the measurement wave front that is undiffracted. To cover the entire area of a mirror of radius a and radius of curvature R, the width of the outermost zone Δr is given by[34]

$$\Delta r \simeq (\lambda/2)(R/a), \tag{10}$$

where the numerical aperture of the zone plate is approximately $\Delta r/\lambda$. Since zone plates are highly chromatic, it is important to limit the number of zones N_z to the inverse of the anticipated relative bandwidth $\Delta\lambda/\lambda$. For interferometry of multilayer coated optics, the relative bandwidth of choice (set by the monochromator) will depend on the number of multilayer pairs and the number of undulator periods and may be chosen to be narrower so as to probe phase effects within the coating. Thus, in differing aspects of this work, we might imagine choosing $\Delta\lambda/\lambda$, and thus N_z, to be somewhere between 30 and 1000. Choosing N_z depending on a specific experiment, we find that the zone plate focal length and radius are given by[34]

$$f \simeq \frac{4N_z(\Delta r)^2}{\lambda}, \tag{11}$$

$$r \simeq 2N_z\Delta r, \tag{12}$$

respectively. For example, a 40-mm-diameter mirror (a = 20 mm) with a radius of curvature of 150 mm requires a 150-μm-diameter zone plate with an outermost zone width of ~50 nm and a total of 500 zones.[35] It would have a focal length of 0.86 mm.

Since the zone plate is at the center of curvature and therefore is imaged onto itself by the mirror, the zone construction (i.e., zone width, zone spacing, circularity) is not overly critical. It is only important that there be 180° symmetry about the center of the zone plate.

As shown in Fig. 6, the zone plate interferometer is best suited for measuring concave mirrors. Measuring convex mirrors and multielement reflective systems is more difficult and requires auxiliary optics, which increases the complexity of the measurement and influences the measurement itself.

Another type of common path interferometer that is more versatile, especially for measuring the wave front of optical systems, is the point-diffraction interferometer.[36] This interferometer produces an interference pattern by using the wave front after it has passed through the optical system. A spherical reference wave front is generated from the aberrated wave front by diffraction. This interferometer, shown in Fig. 7, consists of a partially transparent membrane, perhaps silicon nitride (Si_3N_4), coated with an absorbing layer of aluminum in which a small pinhole has been etched. The radiation from the undulator is focused at one conjugate of the optical system and the point-diffraction interferometer is placed at the other conjugate, as shown in Fig. 8. The diameter of the focused source and pinhole are slightly smaller than the resolution limit of the system. The attenuated (aberrated) wave front transmitted by the membrane interferes with a spherical wave front diffracted by the pinhole. The absorption of the coating is chosen so that the two interfering wave fronts are of approximately equal intensity to ensure high visibility fringes. The transmission ratio of the coated membrane is chosen to be ~ 0.01, which is achieved with approximately 150 nm of aluminum.

To estimate exposure time for interferometry at the ALS, we consider as an example the specific combination of coherent power from an 8.0-cm undulator and use of a zone plate interferometer generically similar to that shown in Fig. 6. For operation at 130 Å, Fig. 4 and the accompanying text indicate a spatially coherent power of 0.2 mW in a relative spectral bandwidth of 10^{-3}, which corresponds to a coherence length of 6.5 μm. We assume that spatially coherent radiation is selected by a pinhole within the monochromator. At 130 Å, this coherent power corresponds to a coherent photon flux of approximately 1×10^{13} photons/s. We estimate the throughput of the zone plate interferometer to be approximately $1/2 \times 10^{-3}$. The throughput estimate is obtained by assuming a beam-splitter efficiency of 1/3 twice (going in and coming out), a zone plate efficiency of 1/20 to first order and 1/2 to zeroth order times 2, since two zone plate orders are used

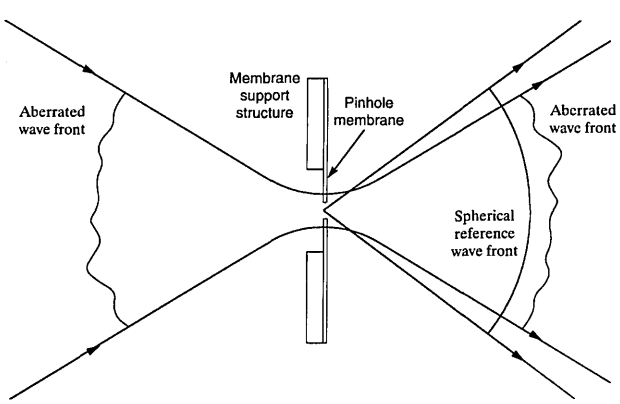

Fig. 7. Details of the point-diffraction interferometer. The spherical reference wave front is generated by diffraction from a pinhole in the partially absorbing membrane.

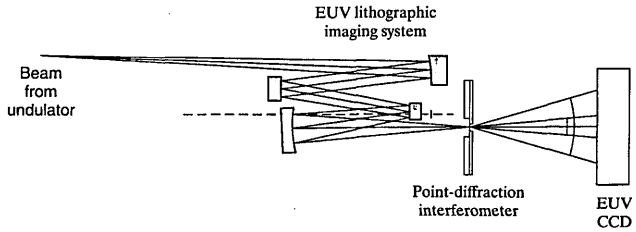

Fig. 8. Point-diffraction interferometer testing of an EUV lithographic imaging system. The source (or its image) and the point-diffraction interferometer are placed at the conjugates of the system.

(test and reference beams), mirror reflectivities of 2/3 twice (the test mirror and the spatial filter mirror), and a back-thinned CCD efficiency of 1/2. If we further assume use of a $10^3 \times 10^3$ CCD array such that available photons are divided into 10^6 separate pixels, then the detected photon flux is estimated to be approximately $(10^{13}$ photons/s$)(10^{-3})(10^{-6})$, or approximately 10^4 photons/s pixel. Assuming that the detection of 10^3 photons/pixel provides statistically useful fringe visibility, the photon flux per pixel estimated above provides an exposure time of $\sim 1/10$ s. Considering the need for real-time measurements, particularly in optical system alignment studies, and the potential for fringe contrast loss because of vibration, exposure times of this order seem appropriate. Further estimates of exposure time, such as an experiment utilizing point-diffraction interferometry of an imaging system, as illustrated in Fig. 8, involve partially offsetting factors that are best deferred to a time when the optical systems themselves are better defined.

Beam Line

The EUV optical transport system following the undulator, including mirrors and apertures (some of which are water cooled), a monochromator, focusing elements, and positioning devices, is generally referred to as a *beam line.* If branching is employed to serve several end stations, the term *branch lines* is employed. Figure 9 shows a diagram of beam-line optics[37,38] capable of providing a narrow bandwidth and a sufficiently small phase space to meet spatial and temporal coherence requirements for experiments such as EUV interferometry. The first mirror is a pop-up planar mirror for branch-line selection as well as for reducing the heat load on the optics to

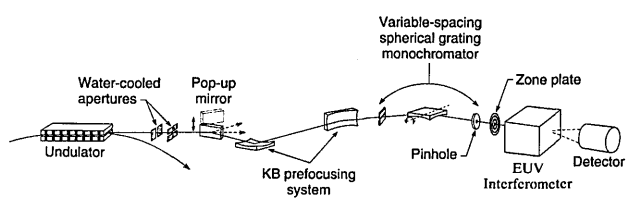

Fig. 9. Preliminary diagram showing beam line optics for the development and the application of EUV interferometry. The design includes water-cooled apertures, a pop-up mirror, a Kirkpatrick–Baez (KB) prefocusing system, a variable-spacing spherical grating monochromator, and an interferometer.

follow. The Kirkpatrick–Baez prefocus system consists of vertical-folding and horizontal-folding spherical (or cylindrical) mirrors that focus the source image vertically on the entrance slit of the monochromator and horizontally on the exit slit (pinhole), respectively. The pinhole serves as the exit slit of the monochromator and can also serve as a spatial filter. The combination of pinhole and zone plate aperture defines the through rays in both real and phase space. By through rays we mean the rays that pass through both the pinhole and the zone-plate aperture. The effective phase space of the through rays is fairly close to that of spatially coherent radiation. The monochromator is a constant-deviation type, equipped with a variable-spacing spherical grating that provides sufficient spectral resolution and temporal coherence for EUV interferometry. The relative spectral bandwidth is variable from 100 to several thousand, depending on the gratings used, permitting bandwidth and coherence length to be traded off with available photon flux. Additional branch lines are anticipated, including one designed for a very narrow relative spectral bandwidth ($\Delta\lambda/\lambda \simeq 3 \times 10^4$) at selected wavelengths.[39,40]

Conclusion

A path toward at-wavelength EUV interferometry of reflective optics and optical systems based on the use of partially coherent undulator radiation is presented. Systems that cover wavelengths from nominally 45 to 400 Å are possible, employing a variety of diffractive and reflective optics. A capability for at-wavelength interferometry would substantially enhance the ability to extend EUV and SXR optics for lithography, microscopy, astronomy, and other emerging applications to these very short wavelengths.

This work was supported by the U.S. Department of Defense, Advanced Research Projects Agency, the U.S. Air Force Office of Scientific Research, and the U.S. Department of Energy, Office of Basic Energy Sciences.

References and Notes

1. D. Attwood, "New opportunities at soft x-ray wavelengths," Phys. Today 45 (8), 24–31 (1992).
2. J. H. Underwood, R. C. C. Perera, J. B. Kortright, P. J. Batson, C. Capasso, S. H. Liang, W. Ng, A. K. Ray-Chaudhuri, R. K. Cole, G. Chen, Z. Y. Guo, J. Wallace, J. Welnak, G. Margaritondo, F. Cerrina, G. De Stasio, D. Mercanti, and M. T. Ciotti, "The MAXIMUM Photoelectron Microscope at the University of Wisconsin's Synchrotron Radiation Center," in *X-Ray Microscopy III,* A. G. Michette, G. R. Morrison, C. J. Buckley, eds. (Springer-Verlag, Berlin, 1992), p. 220.
3. J. E. Bjorkholm, J. Bokor, R. R. Freeman, J. Gregus, T. E. Jewell, W. M. Mansfield, A. A. MacDowell, E. L. Rabb, W. T. Silfvast, L. H. Szeto, D. M. Tennant, W. K. Waskiewicsz, D. L. White, D. L. Windt, O. R. Wood II, and J. H. Bruning, "Reduction imaging at 14 nm using multilayer-coated optics: Printing of features smaller than 0.1 μm," J. Vac. Sci. Technol. B **8,** 1509–1513 (1990).
4. *Physics of Multilayer Structures.* Vol. 7 of 1992 OSA Technical Digest Series (Optical Society of America, Washington, D.C., 1992).
5. D. Stearns, R. S. Rosen, and S. P. Vernon, "High-performance multilayer mirrors for soft x-ray projection lithography," in *Multilayer Optics for Advanced X-ray Applications* N. M. Ceglio, ed., Proc. Soc. Photo-Opt. Instrum. Eng. Proc. **1547,** 2 (1991).
6. E. M. Gullikson, J. H. Underwood, P. C. Batson, and V. Nikitin, "A soft x-ray/EUV reflectometer based on a laser produced plasma source," J. X-Ray Sci. Technol. **3,** 283–299 (1992).
7. D. G. Stearns, R. S. Rosen, and S. P. Vernon, "Normal-incidence x-ray mirror for 7 nm," Opt. Lett. **16,** 1283–1285 (1991).
8. J. B. Kortright, E. M. Gullikson, and P. E. Denham, "Masked deposition techniques for achieving multilayer period variations required for short-wavelength (68-Å) soft-x-ray imaging optics," Appl. Opt. **32,** 6961–6968 (1993).
9. Estimates of future memory chip sizes are based on past trends. For example, see P. Burggraaf, "Lithography's leading edge, part 2: I-line and beyond," Semiconductor Int. **15,** 52–56 (1992).
10. W. T. Welford, *Aberrations of Optical Systems* (Hilger, Bristol, UK, 1986), Chap. 13, p. 241.
11. Assumed independent, random surface figure error to arrive at this estimate.
12. J. Underwood, E. M. Gullikson, and K. Nguyen, "Tarnishing of molybdenum/silicon multilayer x-ray mirrors," Appl. Opt. **32,** 6985–6990 (1993).
13. A. E. Ennos, "Stresses developed in optical film coatings," Appl. Opt. **5,** 51–61 (1966).
14. P. A. Greet, "Coating stress in Fabry–Perot étalons," Appl. Opt. **25,** 3328–3329 (1986).
15. R. R. Kola, D. L. Windt, W. K. Waskiewicz, B. E. Weir, R. Hull, G. K. Celler, and C. A. Volkert, "Stress relaxation in Mo/Si multilayer structures," Appl. Phys. Lett. **60,** 3120–3122 (1992).
16. A. Hofmann, "Quasi-monochromatic synchrotron radiation from undulators," Nucl. Instrum. Methods **152,** 17–21 (1978).
17. B. M. Kincaid, "A short-period helical wiggler as an improved source of synchrotron radiation," J. Appl. Phys. **48,** 2684–2691 (1977).
18. D. F. Alferov, Y. A. Bashmakov, and E. G. Bessonov, "Undulator radiation," Sov. Phys. Tech. Phys. **18,** 1336–1339 (1974).
19. *ALS Handbook,* Pub-643, Rev. 2 (Lawrence Berkeley Laboratory, Berkeley, Calif., 1989).
20. R. P. Walker, "Calculation of undulator radiation spectral and angular distributions," Rev. Sci. Instrum. **60,** 1816–1819 (1989).
21. B. Kincaid, "Random errors in undulators and their effects on the radiation spectrum," J. Opt. Soc. Am. B **2,** 1294–1306 (1985).
22. B. Kincaid, "Analysis of field errors in existing undulators," Nucl. Instrum. Methods A **291,** 363–370 (1990).
23. P. A. Tipler, *Foundations of Modern Physics* (Worth, New York, 1969), p. 209.
24. A. E. Siegman, *Lasers* (University Science, Mill Valley, Calif., 1986), Chap. 17, p. 663. Equation (7) is obtained when propagation is described in terms of $1\sqrt{e}$ measures.
25. M. Born and E. Wolf, *Principles of Optics,* 6th ed. (Pergamon Press, New York, 1984), Chap. 7, p. 316.
26. D. Attwood, K. Halbach, and K. J. Kim, "Tunable coherent x-rays," Science **228,** 1265–1272 (1985).
27. For further discussion, see K. J. Kim, "Characteristics of synchrotron radiation," in *Physics of Particle Accelerators,* M. Month and M. Dienes, eds. (American Institute of Physics, New York, 1989), p. 565.
28. M. C. Hettrick and J. H. Underwood, "Stigmatic high through-

put monochromator for soft x-rays," Appl. Opt. **25,** 4228–4231 (1986).
29. R. L. Kauffman, D. W. Phillon, and R. C. Spitzer, "X-ray production 13 nm from laser-produced plasmas for projection x-ray lithography applications," Appl. Opt. **32,** 6897–6900 (1993).
30. P. Hariharan, *Optical Interferometry* (Academic, New York, 1985).
31. D. Malacara, *Optical Shop Testing* (Wiley, New York, 1992).
32. J. C. Wyant, "Double frequency grating lateral shear interferometer," Appl. Opt. **12,** 2057–2060 (1973).
33. R. N. Smartt, "Zone plate interferometer," Appl. Opt. **13,** 1093–1099 (1974).
34. A. V. Baez, "Fresnel zone plate for optical image formation using extreme ultraviolet and soft x radiation," J. Opt. Soc. Am. **51,** 405–412 (1961); G. Schmahl, D. Rudolph, P. Guttmann, and O. Christ, "Zone plates for x-ray microscopy," in *X-Ray Microscopy,* G. Schmahl and D. Rudolph, eds. (Springer-Verlag, Berlin, 1984), p. 63.
35. E. H. Anderson and D. Kern, "Nanofabrication of zone plates for x-ray microscopy," in *X-Ray Microscopy III,* A. G. Michette, G. R. Morrison, and C. J. Buckley, eds. (Springer-Verlag, Berlin, 1992), p. 75.
36. R. N. Smartt and W. H. Steel, "Theory and application of point-diffraction interferomters," Jpn. J. Appl. Phys. **14** (Suppl. 14-1), 351–356 (1975).
37. W. Meyer-Ilse, M. Koike, R. Beguiristain, J. Maser, and D. Attwood, "X-ray microscopy resource center at the Advanced Light Source," in *Soft X-Ray Microscopy,* C. J. Jacobsen and J. E. Trebes, ed., Proc. Soc. Photo-Opt. Instrum. Eng. **1741,** 112–115 (1992).
38. M. Koike and T. Namioka, "Merit function for the design of grating instruments," Appl. Opt. (to be published).
39. M. C. Hettrick, J. Underwood, P. Batson, and M. J. Eckart, "Resolving power of 35,000 (5 mA) in the extreme ultraviolet employing a grazing incidence spectrometer," Appl. Opt. **27,** 200–202 (1988).
40. M. C. Hettrick, "Surface normal rotation: a new technique for grazing incidence monochromators," Appl. Opt. **31,** 7174–7178 (1992).